

Evolution of A Triad Twisted String Actuator for Controlling a Two Degrees of Freedom Joint to Improve Performance and Allow for Active Transmission Adjustment

Damian Crosby, Joaquin Carrasco *Member, IEEE*, William Heath *Member, IEEE*, and Andrew Weightman

Abstract—actuated universal joint are used in a wide range of robotic applications, including mobile snake robots, snake-arm robots and robotic tails. Depending on the application and design constraints, these can use remote cable or fluid driven systems, or inline motors. In order to realise the benefits of inline actuation while keeping the system compact with a high power to weight ratio, an actuated universal joint was developed using an “antagonistic triad” of three twisted string actuators. However, the design of this system had numerous drawbacks in its current form, namely a limited angle range, poor accuracy due to the angular feedback sensors used, and issues with string failure due to mechanical design choices. In this publication, these drawbacks are addressed through design changes, and angle range was increased from $\pm 14.5^\circ$ to $\pm 0.0^\circ$ for a single axis, and $\pm 6^\circ$ to $\pm 0.0^\circ$ for a dual axis. These changes also allowed the introduction of active transmission adjustment, which allows for changing the transmission reduction during operation, which adjusts the maximum torque and velocity to adapt to different joint loads.

Index Terms—Flexible Robots, Force Control, Tendon/Wire Mechanism, Twisted String Actuator.

I. INTRODUCTION

AUJ mechanisms are found in a wide range of robotic applications that require soft-rigid reconfigurable mechanisms, such as confined space inspection using continuum robots [1], highly manoeuvrable mobile snake robots [2], and biomimetic robot tails for stability [3]. These can either use inline actuators which directly move the joint [4]–[6], or cable/fluid driven systems that rely on a static “base” to house the actuators or compressors [7]. In the former case, this results in high torque requirements for the actuators, as they have to lift the mass of all the actuators in subsequent sections. In the latter case, space is required for the base, which is not practical in all applications, such as mobile robots.

D. Crosby, and A. Weightman are with the Department of Mechanical, Aerospace and Civil Engineering, School of Engineering, Faculty of Science and Engineering, The University of Manchester, Manchester, United Kingdom.

J. Carrasco and W. Heath are with the Department of Electrical and Electronic Engineering, School of Engineering, Faculty of Science and Engineering, The University of Manchester, Manchester, United Kingdom.

First developed by Würtz *et al.* [8] in 2010, the TSA uses two or more strings between two fixtures as a linear actuator. When one fixture is rotated (typically by an electric motor), the looped string twists into a helix, decreasing the distance between them. TSA actuators have been used for a hand orthosis [9], elbow joint [10] and foldable robot arm [11] among other functions.

Whereas alternative electric actuation systems, such as leadscrews, require the addition of gearing for significant increases in reduction (lower velocity, higher torque), which increases actuator size and mass, a TSA can increase reduction by reducing string thickness or string count, which slightly reduces actuator mass [12]. In the case of leadscrews, the reduction can be increased marginally by decreasing thread lead [13], but this can quickly come up against manufacturing tolerances and material stiffness and toughness limitations. The screw radius can also be increased, but this has the effect of increasing actuator size and mass in a similar fashion.

One of the main challenges of TSA is the reduction changes depending on the motor angle (and therefore actuator position). This is an inverse nonlinear relationship, where the function has a decreasing derivative as the motor angle increases [8], [12]. String compliance may also need to be considered under high force conditions, but this can be mitigated with accurate modelling [14], or a suitably robust control strategy that can ignore compliance in its system model [8], [12]. Since strings are not rigid, TSA can only impart force in tension, and 1 degree of freedom (DOF) single TSA actuator joints must make use of a spring return mechanism [15]–[17], which can limit actuator range since the spring force increases as maximum TSA force decreases [18]. Usman *et al.* [18] developed a linear force return mechanism ($k = 0$) to partially mitigate this issue, but an ideal situation is to have a matching antagonistic force profile. This can be done by using a second TSA actuator which is synchronised with the first [10], [19]–[21]. Therefore, by adding a third TSA, a 2 DOF actuator can be realised without the use of springs.

The use of TSA as an actuator for an AUJ is an understudied area of research. Konda, Bombara, Chow, *et al.* [22] have proposed a similar design using a flexible core

with continuous curvature as opposed to a rigid universal joint, which outlines an open loop control solution for multi axis control using only two TSA experimentally demonstrated with a limited azimuthal axis range in polar coordinates. For the first time the authors demonstrate a robust closed loop control of an AUJ in both axes of motion, including the full azimuthal range of $[0, 360]^\circ$, using three TSA in an “antagonistic triad” configuration. The result is a light, compact AUJ design that has the potential to significantly improve upon exiting inline actuation options.

In this publication, the authors aim to improve on the prototype constructed in [23], previously published as a conference proceeding at the IEEE International Conference on Robotics and Automation (ICRA) 2022, by improving the joint angle range, string lifetime, and by introducing ATA, for adjustments to the dynamics of the system in real time both before and during operation. This publication will also conduct additional experiments with increased follower mass and joint velocity, include data to characterise each individual TSA under force control, and expand on the discussions in the conference proceedings with a focus on multi-segment operation.

A. A Twisted string actuator

First developed by Würtz, May, Holz, *et al.* [8] in 2010, TSA uses two or more strings between two fixtures as a 1 DOF linear actuator. When one fixture is rotated (typically by an electric motor), the strings twist into a helix, decreasing the distance between the fixtures, as shown in figure 1. Given the unwound length l_u , and the cross-section radius of the string r_s (or $r_s + r_c$ when there are more than two strings, where r_c is the radius of a tangentially constrained circle drawn between the strings) as shown in figure 2, the actuator length is given by

$$l_s(\theta_s) = \sqrt{l_u^2 - \theta_s^2 r_s^2} \quad (1)$$

where θ_s is the motor angle, as shown in figure 3.

This equation assumes an infinite string stiffness, so is only reasonably accurate under low tension. Although theoretically the stroke of the TSA can be the entire domain of $[0, l_u]$, in reality the thickness of the string prevents a geometric helix from forming once the helix pitch $q < 4r_s$ (or $q < 2nr_s$ for n strings). This limits the lower bound of the stroke as follows,

$$l_{min} = \frac{l_u}{\sqrt{\frac{\pi^2}{2} + 1}} \approx 0.46 l_u \quad (2)$$

or approximately 46% of l_u for a two string TSA.

B. Antagonistic Triad

As mentioned in the introduction, three TSA can operate an “antagonistic triad”, analogous to the antagonistic pairs for 1 DOF joints used in [10], [19]–[21]. These are arranged at three equidistant points around a circle of radius r , to form two equilateral triangles at either end

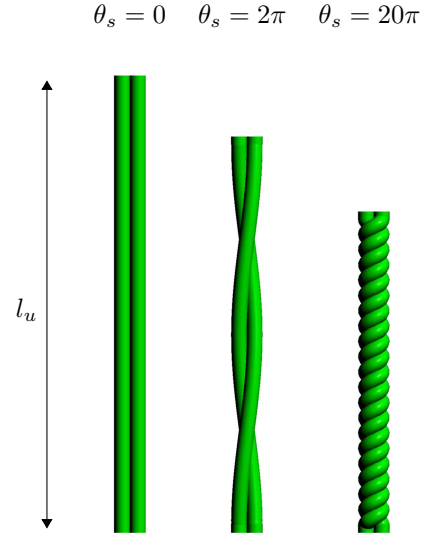


Fig. 1: The value of θ_s increases the number of twists in a string bundle with a string length l_u .

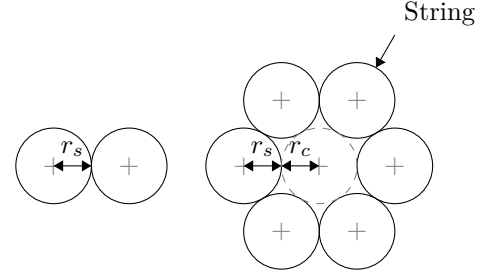


Fig. 2: The location of r_s and optionally r_c in a string bundle.

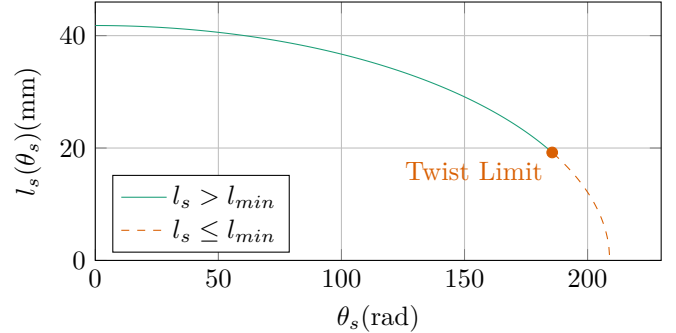


Fig. 3: TSA string length against motor angle with coefficients from table I.

of the linear actuators. The centers of the circles are connected along their normal axes to a universal joint, with a magnitude of l_1 from the universal joint to the start of the actuators, and l_2 from the universal joint to the end. This geometric construction is shown in figure 4. If $\boldsymbol{\theta} = [\theta_1 \ \theta_2]^\top$ is defined as the rotation of the universal joint on the x and y axes in the coordinate system at the start of the actuators, such that the normal vectors are collinear when $\boldsymbol{\theta} = [0 \ 0]^\top$, then the magnitude for the

vector between each pair of points at either end of the actuator can be calculated using

$$\begin{aligned}\lambda_1(\boldsymbol{\theta}) &= \sqrt{a + 2l_1r \sin(\theta_2) \cos(\theta_1) + l_2^2} \\ \lambda_2(\boldsymbol{\theta}) &= \sqrt{a + b + c - d} \\ \lambda_3(\boldsymbol{\theta}) &= \sqrt{a - b - c + d}\end{aligned}$$

where:

$$\begin{aligned}a &= l_1^2 + 2l_1l_2 \cos(\theta_1) \cos(\theta_2) \\ b &= \sqrt{3}l_1r \sin(\theta_1) - l_1r \sin(\theta_2) \cos(\theta_1) + l_2^2 \\ c &= \sqrt{3}l_2r \sin(\theta_1) \cos(\theta_2) - l_2r \sin(\theta_2) \\ d &= \frac{\sqrt{3}r^2 \sin(\theta_1) \sin(\theta_2)}{2} - \frac{3r^2 \cos(\theta_1)}{2} - \frac{r^2 \cos(\theta_2)}{2} + 2r^2.\end{aligned}\quad (3)$$

where $\Lambda(\boldsymbol{\theta}) = [\lambda_1(\boldsymbol{\theta}) \quad \lambda_2(\boldsymbol{\theta}) \quad \lambda_3(\boldsymbol{\theta})]$ is a vector function which outputs the magnitudes of each point pair, and therefore the lengths of each actuator, assuming both ends of each actuator can rotate freely on both x and y axes. The output of this equation is plotted in figure 5 for a domain of $[-\frac{\pi}{2}, \frac{\pi}{2}]$, with coefficients from table I.

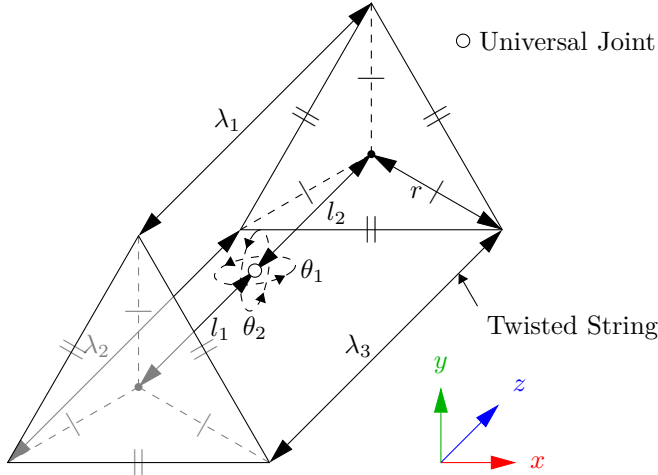


Fig. 4: Kinematic diagram of the antagonistic triad, where the universal joint rotation is defined by $\theta_{1,2}$ on the y and x axes respectively, and the actuator lengths are defined by $\lambda_{1,2,3}$ for the *top*, *left* and *right* strings. r and $l_{1,2}$ define the anchor points of the strings.

II. CONTROL SYSTEM

While position control for 1 DOF TSA joints, both spring return [24] and antagonistic [25], is possible, it proved too unstable to be used for the antagonistic triad. Therefore a force control system was designed for each TSA using a simple P controller, which a position control system would cascade down to, by converting the setpoint angle of the AUJ into three force setpoints for each TSA. This was done by first converting the angular velocity from the AUJ position PID controller to a setpoint AUJ torque using inverse dynamics [26]. A force optimisation algorithm from [27] was then implemented that takes the

desired AUJ joint torque as an input and outputs a tensile force setpoint for each TSA.

This control system functions because each TSA has a tensile force when $l_s(\theta_s) < \lambda_n(\boldsymbol{\theta})$, which is calculated as the difference in triad length and TSA contraction length multiplied by the load stiffness $(\lambda_n(\boldsymbol{\theta}) - l_s(\theta_s))K_L$. When all of the TSA tensile forces are equal, there is no torque on the AUJ, but when they are unequal, a torque is generated, and if these torques do not match the torques required by the current dynamics to maintain the AUJ orientation, the AUJ will rotate. As the tensile force is measured using load cells, the control system does not need to know the value of K_L since a setpoint force can be maintained using a P controller.

This control system can be split up into four functions:

- 1) C_1 AUJ Position PID Controller with Acceleration Feedforward
- 2) C_2 Inverse Dynamics
- 3) C_3 TSA Force Optimisation Algorithm
- 4) C_4 TSA Force P Controller

These functions are nested into a cascade function shown in figure 7.

A. AUJ Position PID Controller with Acceleration Feed-forward

Firstly, a PID controller is used to generate a control signal \mathbf{u} with the desired AUJ angular position and velocity $\mathbf{q}, \dot{\mathbf{q}}$ as the setpoint. The current AUJ angular position $\boldsymbol{\theta}$ and velocity $\dot{\boldsymbol{\theta}}$ as feedback, plus the addition of a feedforward term for the desired input acceleration $\ddot{\mathbf{q}}$. $\dot{\mathbf{q}}$ and $\ddot{\mathbf{q}}$ can be pre-programmed as part of a second order trajectory profile, or can be calculated from a ramp generator when \mathbf{q} is manually controlled.

In the discrete implementation used for fixed step simulation and experimental system control, the integral term of the PID is replaced by the trapezoidal rule.

B. Inverse Dynamics

The control signal \mathbf{u} from the PID controller is then converted to the desired AUJ torque $\boldsymbol{\tau}$. This is achieved using the Euler-Lagrange formulation which takes into account the dynamic properties of the AUJ in its current state, as shown in figure 6. For simplicity, the mass of the universal joint is ignored in the calculations and the value of the follower COM relative to the universal joint pivot ρ only has a z component, ρ_3 , which is included in the experiments in section IV-C4 but set to zero for all other experiments. The torque is calculated as $\boldsymbol{\tau} = D(\boldsymbol{\theta})\mathbf{u} + C(\boldsymbol{\theta}, \dot{\boldsymbol{\theta}})\dot{\boldsymbol{\theta}} + G(\boldsymbol{\theta})$ where the functions D , C , and G are given in (4).

C. TSA Force Optimisation Algorithm

This uses the *inverse force transformation* algorithm from [27] with the jacobian in equation 3 to select an optimal force vector from the desired joint torque. Here it is presented in an unexpanded and more general form,



Fig. 5: Surface plots of each element of the vector function $\Lambda(\theta)$, assuming coefficient values from table I. For every pair of universal joint angles θ , there is a corresponding vector of actuator lengths $\Lambda(\theta)$. Note that λ_2 and λ_3 are symmetric.

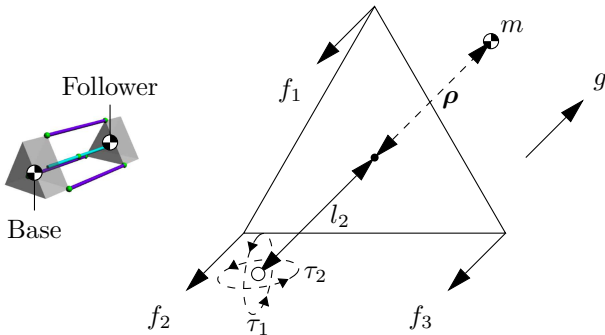


Fig. 6: Dynamics of an antagonistic triad based on figure 4, where the follower mass is m , the follower center of mass (COM) relative to the universal joint pivot is ρ , the forces on each anchor point are $f_{1,2,3}$ and the universal joint torque is $\tau_{1,2}$.

$$\begin{aligned} J_\Lambda &= \begin{bmatrix} \frac{\partial \lambda_1}{\partial \theta_1} & \frac{\partial \lambda_2}{\partial \theta_1} & \frac{\partial \lambda_3}{\partial \theta_1} \\ \frac{\partial \lambda_1}{\partial \theta_2} & \frac{\partial \lambda_2}{\partial \theta_2} & \frac{\partial \lambda_3}{\partial \theta_2} \end{bmatrix} \\ \gamma(i) &= -J_{\Lambda_{-i,*}}^{-T} \left(J_{\Lambda_{i,*}}^T f_{min} + \tau \right) \\ F(\tau, \theta) &= \begin{bmatrix} f_{min} & \gamma(2)_1 & \gamma(3)_1 \\ \gamma(1)_1 & f_{min} & \gamma(3)_2 \\ \gamma(1)_2 & \gamma(2)_2 & f_{min} \end{bmatrix}. \end{aligned} \quad (5)$$

A force matrix F is created from the torque input τ , jacobian J_Λ from the vector function Λ as defined in equation 3, and minimum force constant f_{min} . f_{ii} is equal to f_{min} , while the other elements in the column are based on a calculation using $J_{\Lambda_{-i,*}}$ where $-i$ is a row removed from the matrix. Algorithm 1 is then used to create output force vector f , which minimises the net force on all TSA while producing the desired output torque on the universal joint.

D. TSA Force Proportional Controller

The selected forces are then used as an input to a P controller with gain k_{ps} using the measured load cell forces \mathbf{f}_{act} as feedback. The output from this can then be used to control the top, left and right TSA motors, corresponding

Algorithm 1 Selects one column of F to be the output force vector f , where \top and \perp are boolean *true* and *false* respectively, and $f_{*,i}$ is the i th column of F .

```

1:  $s \leftarrow [\top \ \top \ \top]$ 
2: if  $f_{23} > f_{min}$  then  $s_2 \leftarrow \perp$  else  $s_3 \leftarrow \perp$  end if
3: if  $f_{31} > f_{min}$  then  $s_3 \leftarrow \perp$  else  $s_1 \leftarrow \perp$  end if
4: if  $f_{12} \geq f_{min}$  then  $s_1 \leftarrow \perp$  else  $s_2 \leftarrow \perp$  end if
5: for  $i = 1$  to  $3$  do
6:   if  $s_i \rightarrow \top$  then  $f_{set} \leftarrow f_{*,i}$  end if
7: end for

```

to the actuators in figure 4. A deadband controller was used to compensate for motor limitations, which is further discussed in section IV-B1.

III. SIMULATION DESIGN

To design and refine the parameters of the control system, a Simscape Multibody™ model of the antagonistic triad and control system was created in MATLAB®/Simulink™. This allowed for model design coefficients $l_{1,2}$ and controller gains k_p, k_i, k_d, k_{ps} to be optimised in order to have the most stable control within design limits, as shown in table II.

In the spirit of [8], each TSA was modelled as a state-space system with saturation function $\text{sat}_x^y z = \max(x, \min(y, z))$, and a state-space representation given by

$$\begin{aligned} h(\theta_s) &= \frac{\theta r_s^2}{\sqrt{l_u^2 - \theta_s^2 r_s^2}} \\ k(\theta_s, \theta) &= \lambda_n(\theta) - \sqrt{l_u^2 - \theta_s^2 r_s^2} \\ \dot{x} &= \begin{bmatrix} x_2 \\ -\frac{K_L}{J} h(x_1) k(x_1, \theta) - \frac{C}{J} \text{sgn}(x_2) \end{bmatrix} + \begin{bmatrix} 0 \\ \frac{K_t}{J} \end{bmatrix} u \\ y &= K_L \text{sat}_0^\infty k(x_1, \theta), \end{aligned} \quad (6)$$

which takes motor current u as an input and outputs y as the TSA tension force, where J is the motor inertia, C is the motor coulomb friction (modified from viscous friction as the motor only has dry friction), K_t is the motor torque constant, and K_L is the load stiffness. As

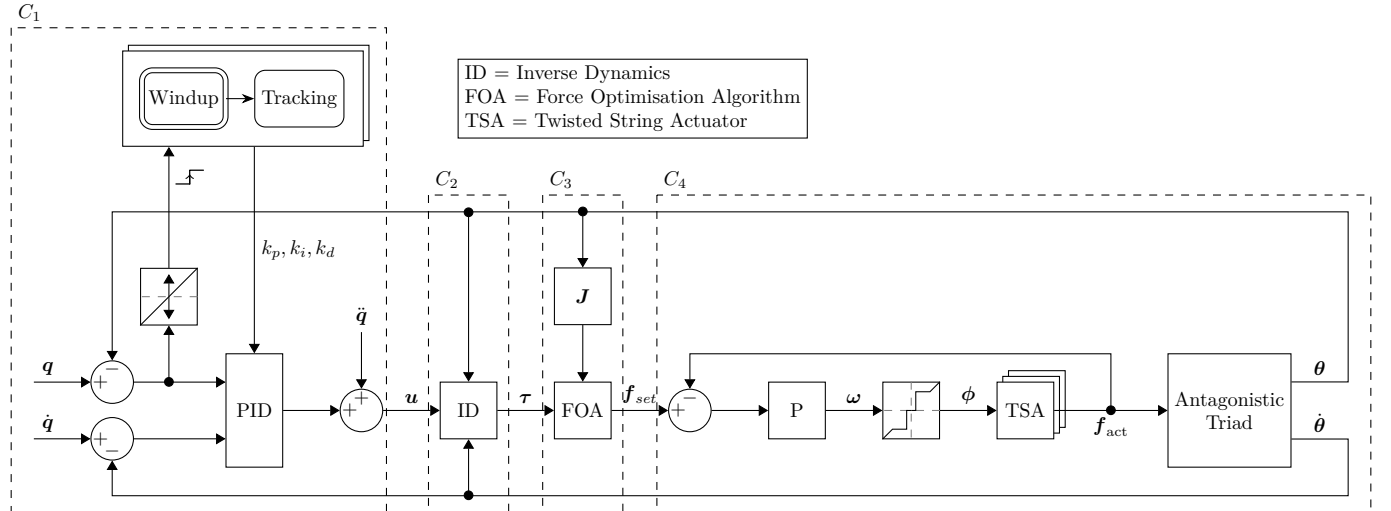


Fig. 7: Block diagram of the complete experimental control system, excluding the hardware velocity controllers for the motors. Dashed boxes correspond to the control functions $C_1 \dots 4$ specified in section II.

$$\begin{aligned}
 D(\theta) &= \text{diag} \left(\begin{bmatrix} I_{22} \cos^2 \theta_2 - I_{33} \cos^2 \theta_2 + I_{33} + l_2^2 m \cos^2 \theta_2 + 2l_2 m \rho_3 \cos^2 \theta_2 + m \rho_3^2 \cos^2 \theta_2 \\ I_{11} + l_2^2 m + 2l_2 m \rho_3 + m \rho_3^2 \end{bmatrix}^\top \right) \\
 C(\theta, \dot{\theta}) &= \begin{bmatrix} \frac{(-I_{22} + I_{33} - l_2^2 m - 2l_2 m \rho_3 - m \rho_3^2) \sin(2\theta_2) \dot{\theta}_2^2}{2} & \frac{(-I_{22} + I_{33} - l_2^2 m - 2l_2 m \rho_3 - m \rho_3^2) \sin(2\theta_2) \dot{\theta}_1^2}{2} \\ \frac{(I_{22} - I_{33} + l_2^2 m + 2l_2 m \rho_3 + m \rho_3^2) \sin(2\theta_2) \dot{\theta}_1^2}{2} & 0 \end{bmatrix} \\
 G(\theta) &= [-gm(l_2 + \rho_3) \sin \theta_1 \cos \theta_2 \quad -gm(l_2 + \rho_3) \sin \theta_2 \cos \theta_1]
 \end{aligned} \tag{4}$$

the original definition is for a fixed load l_u distance from the motor a modified model is required which takes into account the varying length between the motor and load defined by $\Lambda(\theta)$.

The saturation function is used to prevent incorrect compression forces when the string is slack. All of the motor coefficients were taken from the Faulhaber 1724TSR datasheet [28] as this is the motor used in the experimental model. An estimated value is used for the load stiffness, this was chosen to be a high number as the model is expected to be very stiff.

The state space model was then adapted to include constraints on motor velocity and acceleration set by the motor controller in order to keep the motor within design limits $\dot{x}' = [\text{sat}_{-\omega_s}^{\omega_s} \dot{x}_1 \quad \text{sat}_{-\alpha_s}^{\alpha_s} \dot{x}_2]^\top$, which replaces \dot{x} with \dot{x}' , which contain saturation functions for maximum motor velocity v_s and acceleration α_s .

Based on a combination of simulation modelling, motor parameters, and physical design constraints, the model parameters were set to the values in table I. l_2 was set to zero, as this produced the most stable control system in simulation.

TABLE II: PID gains in the simulation and experiment.

Gain	Value	
	Simulation	Experiment*
k_p	800	3×10^4
k_i	3000	350
k_d	50	50
k_{ps}	19	100

* Tracking mode, see section IV-B2.

IV. EXPERIMENTS

TABLE I: Model coefficients.

Coefficient	Value	Coefficient	Value
l_1	41.8 mm	J	$1 \times 10^{-6} \text{ kg m}^{-2}$
l_2	0 mm	K_L	1000 N m^{-1}
r	13 mm	f_{min}	3 N
l_u	41.8 mm	ω_s	441.9 rad s^{-1}
r_s	200 μm	I_s	0.19 A
m	72.619 13 g	K_t	$0.0263 \text{ N m A}^{-1}$
C	0.1315 N mm	τ_s	4.5 mN m
α_s	$1 \times 10^5 \text{ rad s}^{-2}$	ρ	$[0 \quad 0 \quad 0] \text{ mm}$

Coefficient	Value
I	$\begin{bmatrix} 3 \times 10^{-5} & 0 & 0 \\ 0 & 3.2 \times 10^{-5} & 0 \\ 0 & 0 & 1.4 \times 10^{-5} \end{bmatrix} \text{ kg m}^{-2}$

For the experimental validation, a single segment physical prototype of the mechanism was constructed with coefficients from table I as design parameters. This was mounted vertically, in order for the inertial measurement unit (IMU) to measure the orientation of the universal joint. The TSA mechanisms consist of a compact high torque motor attached to the base segment, with a string clamp attached to the motor shaft. On the follower segment, a load cell is mounted on top of a universal joint to ensure a purely axial load, with a capstan bolt attached to the load cell. The string itself is attached to the clamp at both ends using two grub screws for extra security and easy adjustment, and looped through the hole in the capstan bolt. The total mass of the prototype, excluding the mount, is approximately 176 g. Figures 8 and 9 detail the construction of the experiment with all the constituent parts.

The motors were controlled by Fauhaber MCDC3002 motor controllers, which could interface with a National Instruments MyRIO-1900 via the USB port, using a USB to serial converter. The main control loop of the MyRIO was operated at a frequency of 5 Hz. The load cells were Futek LCM100 miniature load cells, selected for their small size with a diameter of only 9.5 mm. The range of the load cells was $\pm 9.8 \text{ N}$ (1 kg), with a sensitivity of 1 mV V^{-1} [29]. The signals from these were amplified using Flyde FE-359-TA instrumentation amplifiers and decoded using an external AD7606 ADC with a 14-bit resolution [30] before being fed into the MyRIO using SPI. The orientation of the AUJ was measured using a Bosch Sensortec BNO080 IMU using the accelerometer data. Due to the poor resolution of the IMU data, which is discussed in section V-D, the pitch and roll data in figures 15 to 19 have a Savitsky-Golay filter applied with a window length of 11 and an order of 1.

A. Force Proportional Controller & Motor Characterisation

Before verifying robust control of the AUJ, the control of each individual TSA needed to be tested in order to characterise the performance of the motors and to ensure the inner loop control system was robust. This would involve selecting the control strategy that gave the best performance. A test force trajectory consisting of a smooth ramp followed by a sine wave was fed into a single tsa force setpoint as $f_{\text{set}}(t)$. The inner loop operated at a frequency of 100 Hz. Each control strategy was tested, and in the end the velocity control strategy proved most optimal, as is shown in figure 13. The results of a sinusoidal force trajectory for the velocity control strategy is shown in figure 14. As can be seen in the inset, there is a nonlinear friction effect which causes a sawtooth like effect on the measured force. This means the motor angle has to be constantly adjusted even with a constant force input, in order to maintain the setpoint force.

1) *Direct current controller*: This strategy takes a pre-set velocity $\dot{\theta}_{\text{set}} \in [0, 4220] \text{ r min}^{-1}$ and uses a hardware

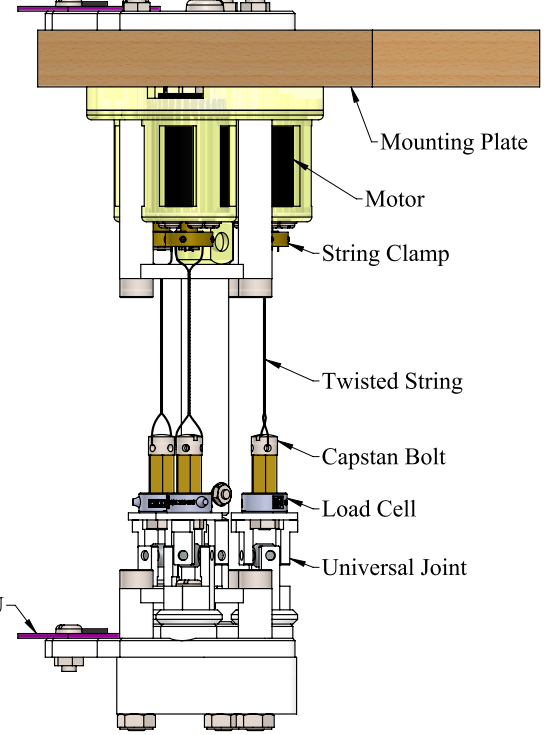


Fig. 8: Schematic of the single segment physical prototype antagonistic triad with labelled components.

PI controller with velocity feedback $\dot{\theta}_{\text{act}}$ to generate a control voltage. This voltage V is then multiplied by the signum of the signal from the proportional force controller in order to ensure the motor spins in the right direction, and then passed to a current limiter with the current error (the proportional force controller signal with the actual current I_{act} subtracted) as the limit, before being sent to the motor. This ensures the motor stops spinning when the target current is reached. V_{lim} is calculated as

$$\begin{aligned}\epsilon_{\dot{\theta}} &= \dot{\theta}_{\text{set}} - \dot{\theta}_{\text{act}} \\ \epsilon_f &= f_{\text{set}} - f_{\text{act}} \\ V_{\text{lim}} &= \left(k_{p_c} \epsilon_{\dot{\theta}} + k_{i_c} \int_0^t \epsilon_{\dot{\theta}} \right) \text{sgn}(k_{p_s} \epsilon_f) \zeta((k_{p_s} \epsilon_f) - I_{\text{act}}),\end{aligned}\quad (7)$$

where k_{p_c} and k_{i_c} are the hardware controller PI constants, k_{p_s} is the force P constant, $\dot{\theta}_{\text{set},\text{act}}$ and $f_{\text{set},\text{act}}$ are the TSA motor velocity and string tension setpoints and responses respectively, and $\zeta(\dots) \in [0, 1]$ is an unknown hardware function that limits the motor voltage depending on the current error. A block diagram of this strategy is shown in figure 10.

2) *Proportional Current Controller*: This strategy is a more direct method of current control, using a software P controller to directly set the voltage of the motor, using the MCDC 3002 as simply a power amplifier. In this case the current error is passed directly to a P controller which has its output limited to prevent damage to the motors.

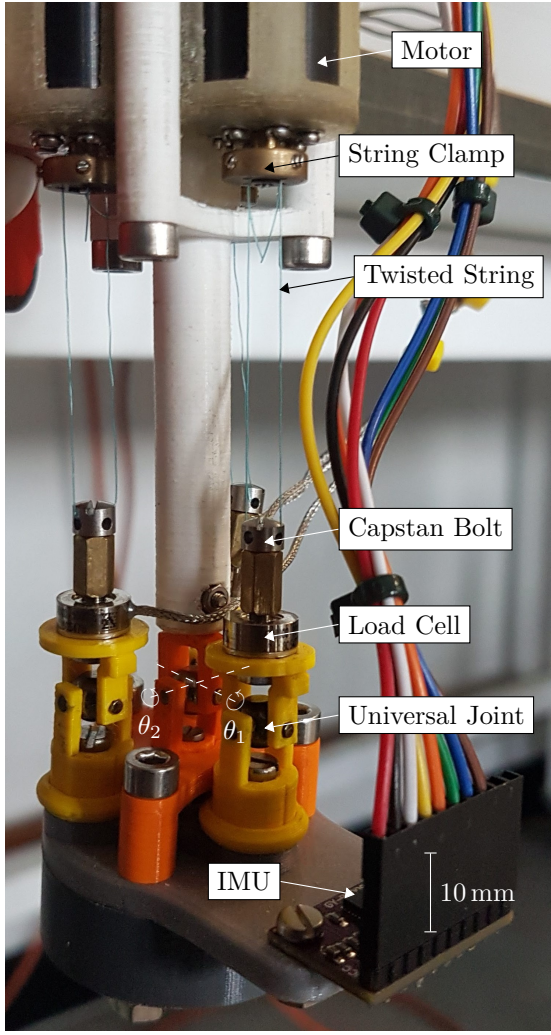


Fig. 9: Annotated photograph of the single segment physical prototype antagonistic triad, with the roll θ_1 and pitch θ_2 axes marked.

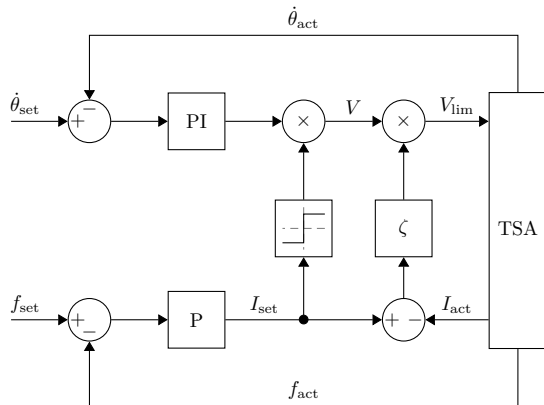


Fig. 10: Block diagram of the direct current controller.

V is calculated as $V = k_{ps}\epsilon_f - I_{act}$. A block diagram of this strategy is shown in figure 11.

3) *Velocity Control*: This strategy simply uses the result of the P controller as a velocity setpoint using the hardware velocity PI controller. V is calculated as $V =$

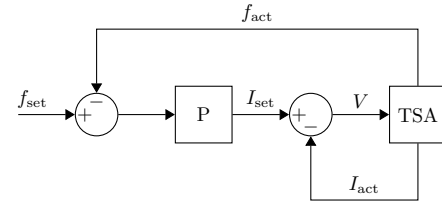


Fig. 11: Block diagram of the proportional current controller.

$k_{pc} (k_{ps}\epsilon_f - \dot{\theta}_{act}) k_{ic} \int_0^t (k_{ps}\epsilon_f - \dot{\theta}_{act}) dt$. A block diagram of this strategy is shown in figure 12.

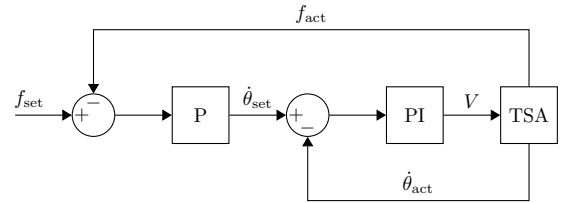


Fig. 12: Block diagram of the velocity controller.

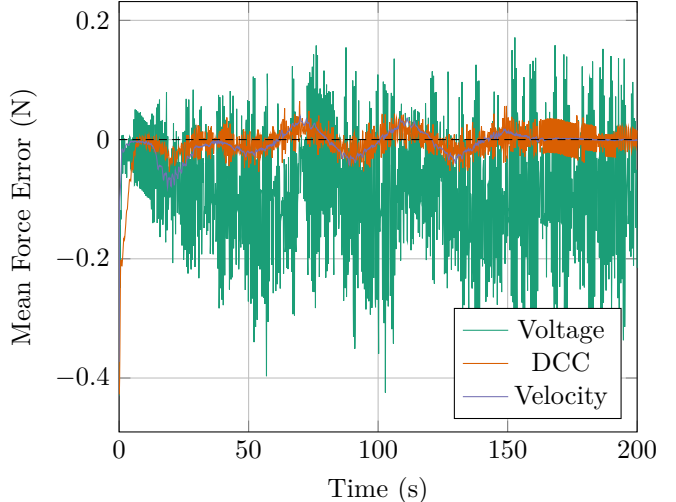


Fig. 13: Mean tracking error for each control strategy.

B. Modifications to Control System

1) *Experimental Velocity Control with Deadband Compensation*: Due to a controller deadband within $\pm 10 \text{ min}^{-1}$, an adjustable deadband compensator is used,

$$\phi_i(\omega_i) = \begin{cases} 10 & h < \omega_i \leq 10 \\ -10 & -10 \leq \omega_i < -h \\ 0 & -h \leq \omega_i \leq h \\ \omega_i & \text{otherwise} \end{cases} \quad (8)$$

where ϕ_i is the compensator for the controller i . An adjustment value $h \in [0, 10]$ changes the threshold at which the compensator switches on and off, allowing for a small deadband to remain.

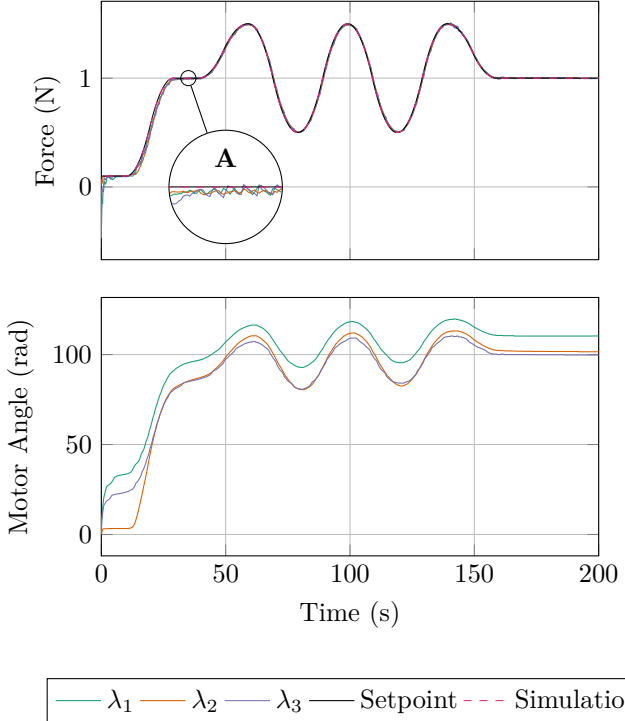


Fig. 14: Load cell, motor angle, and motor velocity signal plot from each string using the velocity control strategy for an experimental trajectory. Inset A shows a zoomed in portion of the graph, illustrating the nonlinear phenomenon noticed in the load cell measurements.

2) *Windup & Tracking States:* When the mechanism is started with the TSA in a completely unwound state, before it can begin tracking a motion trajectory, the TSA strings must “wind up” to closely match the initial state of \mathbf{f} . During this phase, the outer PID gains k_p, k_i are unsuitable and can result in damage to the mechanism. To mitigate this, two sets of PID gains are chosen, one for the windup state ($k_p = 800, k_i = 3000$), and another for the tracking state ($k_p = 3 \times 10^4, k_i = 350$), which the windup state transitions to once suitable stability is achieved. This transition trigger is defined on a per-axis basis, as the first zero crossing of the angle error (as $\mathbf{q} = 0$ this is effectively $\boldsymbol{\theta}$). A graph showing the difference this state change makes to the AUJ orientation is shown in figure 15.

C. Actuated universal joint Experiments

1) *Actuated universal joint Angle Tracking:* Figure 16 plots the tracking response of both the simulation and experiment. Three trajectories were created to test the capabilities of the mechanism. Two were only in one axis of the Universal Joint, and the third was in both axes.

2) *The Effect of f_{\min} on AUJ Roll Range Limits:* Ultimately the AUJ range limits are determined by the angle at which one or more of the TSA are “fully unwound” where $l_s(\theta_s) = l_u$, or “fully wound” where $l_s(\theta_s) = l_{\min}$, unless there is a string failure before this limit. If f_{\min}

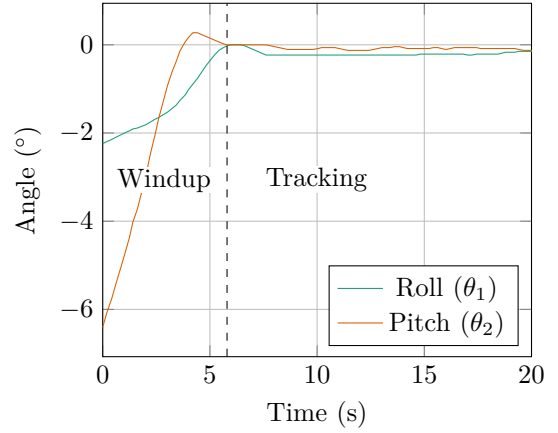


Fig. 15: The initial startup of the mechanism showing the transition between “windup” and “tracking” states.

is increased, the length of each TSA at $\boldsymbol{\theta} = [0, 0]$ is reduced, as a greater difference between $\lambda_n(\boldsymbol{\theta})$ and $l_s(\theta_s)$ is needed for a larger tensile force, as described in section II. Therefore, increasing f_{\min} should increase the AUJ angle range as there is a greater difference between the length of the TSA at $\boldsymbol{\theta} = [0, 0]$ and a fully unwound TSA, as long as there is sufficient length available so an antagonist TSA doesn’t become fully wound.

An experiment was set up where the setpoint angle of the AUJ would continually linearly increase, after a short period of acceleration, on the roll (θ_1) axis. The control system monitored the motor angles of each TSA, and halted the experiment when any TSA motor angle was at or below 2π , as a safety margin to prevent damage to the mechanism. The AUJ angle at the end of the experiment was recorded, as shown in figure 17. By repeating the experiment with increasing values of f_{\min} , it was possible to determine how it affected the maximum roll angle. These experiments were able to achieve modest increases of $4.004^\circ \text{ N}^{-1}$ for the positive (upper) limit of the universal joint roll θ_1 , and $-6.062^\circ \text{ N}^{-1}$ for the negative (lower) limit, within the f_{\min} interval [3, 3.5]. Attempts to increase the upper bound of this interval resulted in string failure, possibly due to $l_s(\theta_s)$ exceeding l_{\min} but it was not possible to conclusively determine this. Similar experiments for the pitch angle resulted in string failure before any TSA fully unwound even at $f_{\min} = 3$.

A better solution for increasing AUJ range limits is to reduce the value of r , as is discussed in section V-C.

3) *The Effect of AUJ Angular Velocity on AUJ Angle Tracking:* To verify the performance of the AUJ at higher angular velocities, the single axis experiments from section IV-C1 were repeated with a trapezoidal “chirp” signal, with the maximum angular velocity increasing by $\omega_0 + (2(n-1)\omega_0)$ each cycle, where n is the cycle number, and ω_0 is the initial maximum angular velocity, and the angular acceleration increasing by $\alpha_0 + (16(n-1)\alpha_0)$ each cycle, where α_0 is the initial angular acceleration. A total of four cycles were performed, with the maximum velocity and acceleration values shown in table III. Figure 18 shows

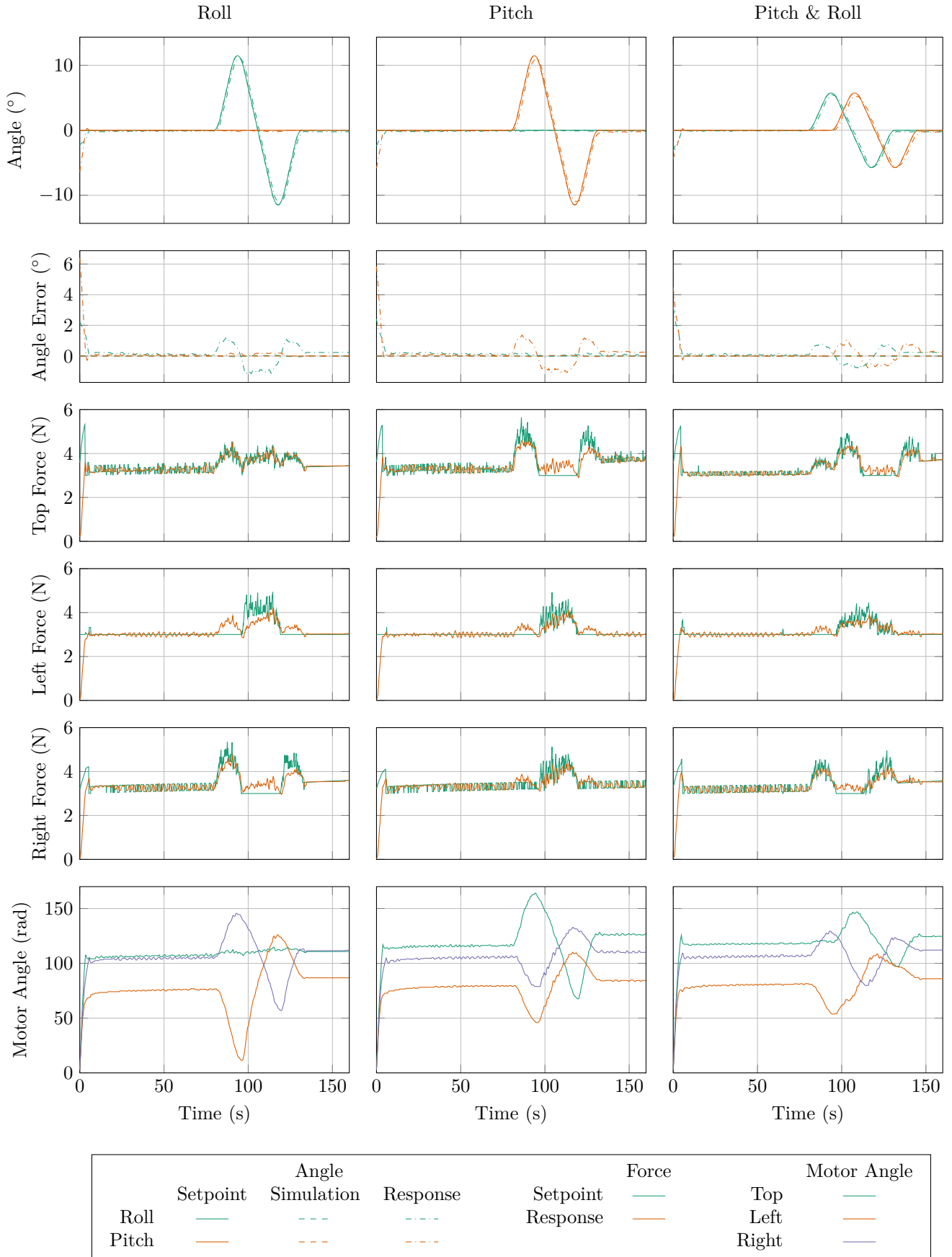


Fig. 16: Plots of the response for three different trajectories, one on only the roll axis θ_1 (column 1), one on only the pitch axis θ_2 (column 2), and one on both axes θ_1 and θ_2 (column 3). Plots include AUJ orientation, forces at the top, left and right TSA, and the motor positions. Note the simulation error is very small, so the plot cannot be seen on the graph.

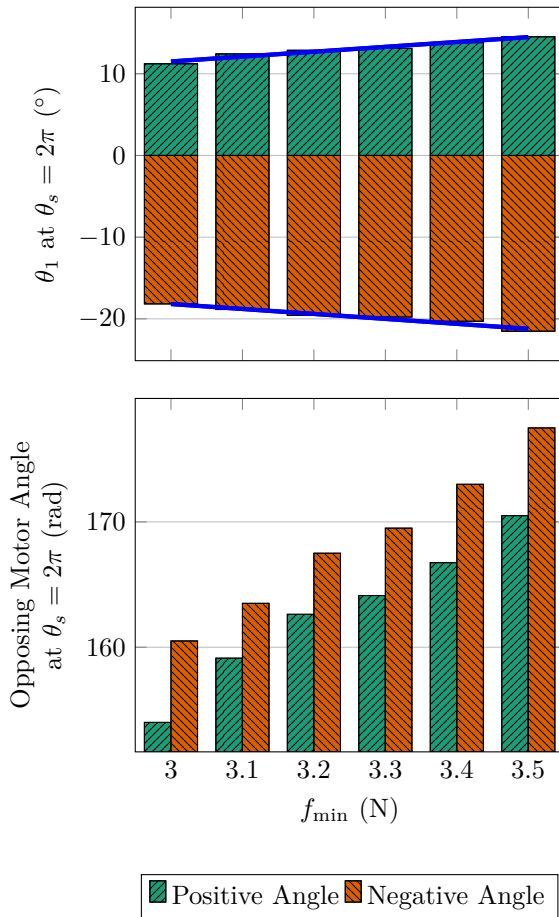


Fig. 17: AUJ roll angle (θ_1) when the smallest TSA motor angle is equal to 2π , and motor angle of the “opposing” TSA (the TSA with the largest motor angle) at the same position.

TABLE III: Trapezoidal trajectory sequence parameters.

Cycle	Max./Min. Angle [rad]	Max. Velocity [rad s ⁻¹]	Acceleration [rad s ⁻²]
1	0.2	0.01	0.00125
2	0.2	0.03	0.02125
3	0.2	0.05	0.04125
4	0.2	0.07	0.06125

the results of these experiments, which shows the tracking error increasing marginally as maximum angular velocity and acceleration increases.

4) *The Effect of Follower Mass on AUJ Angle Tracking:* In order to demonstrate the feasibility of a multiple joint system, additional mass was added to the follower segment and the *Pitch & Roll* trajectory was performed to analyze the effect of the additional mass on the control system. This was performed by the modification of the end of the follower segment to allow multiple standard disc weights, each with a mass of 100 g, to be attached. Four experiments were performed, one with no disc weights attached, and three with one, two, and three disc weights attached, adding approximately 100 g each time. 3D printed custom length spacers were used to maintain an approximately

equal COM for each of the experiments with disc weights. Table IV lists the four follower mass configurations that were tested, with follower mass and inertia matrix m and I , and follower COM z component ρ_3 , along with a figure for each configuration. The follower COM x and y components were set to 0 for these experiments, as they did not vary significantly between experiments, and had a negligible contribution to the dynamics. These figures are based on estimates from a computer aided design (CAD) model developed in SolidWorks®, with known weights of 100 g. Any inertial terms less than 1×10^{-5} were rounded down to 0, which resulted in a diagonal inertia matrix. For each experiment, the inverse dynamics parameters m and ρ were updated so the correct setpoint torque would be calculated.

Figure 19 shows the setpoint and response trajectory for each experiment. Initially, k_p was set to the same value as in table I, however the system was unable to reach a steady state in any configuration other than “No Mass”. Reducing k_p to 1000 in the weighted configurations solved the steady state issue and resulted in an average maximum tracking error of 0° over all configurations with added mass, similar to the result from the initial experiments. However, for the “No Mass” configuration, $k_p = 1000$ resulted in a very poor tracking response, whereas k_p from table I resulted in a maximum tracking error of 0° , once again similar to the result from the initial experiments. In future implementations gain scheduling can be employed to select the most optimal k_p for a given follower mass, that allows for the smallest tracking error while being able to reach a steady state.

V. DISCUSSION

A. TSA Comparison with Leadscrew and Direct Drive

To compare the performance of a TSA AUJ against alternatives, we can measure two metrics, the maximum tension force f_{max} and maximum stroke velocity \dot{p}_{max} . This corresponds to the equivalent of maximum torque and maximum velocity in a rotary motor, a larger f_{max} would be able to actuate a larger follower mass, and a larger \dot{p}_{max} would be able to rotate the AUJ more quickly. The alternatives chosen for comparison are leadscrews of various rod diameters d_n and pitches λ , and a “direct drive” where the motor is rotating the universal joint directly without any reduction or motion transformation, as shown in figure 20.

1) *Twisted string actuator:* For the TSA metrics, the equations from [8], in particular $h(\theta)$ and $k(\theta)$ as used for the state space, which can be used to determine f_{max} and \dot{p}_{max} . By extracting coefficient r_s as an input to make $f(p, r_s)$ and $\dot{p}(\theta, p, r_s)$ the performance of different string thicknesses can be compared for a given unwound length l_u and $\tau_{max}, \dot{\theta}_{max}$ over the range of the contraction length p . f_{max} is calculated as

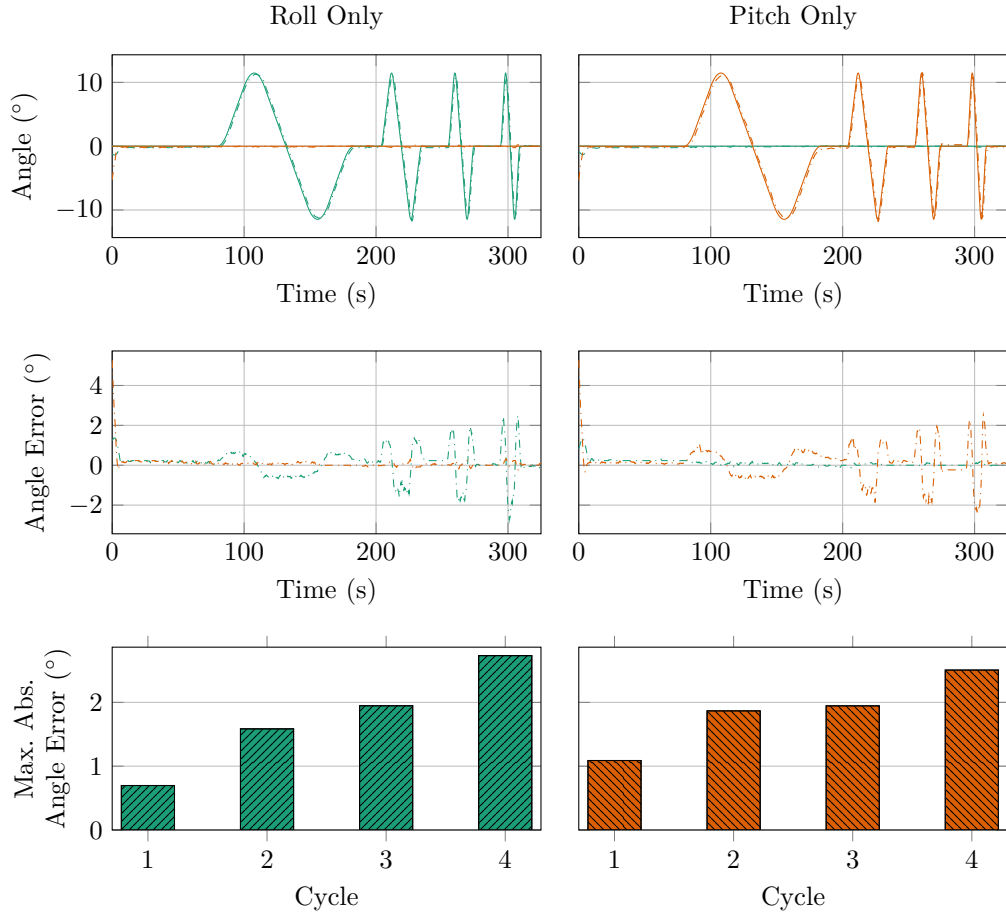


Fig. 18: Results of the trapezoidal velocity trajectory from table III for both AUJ pitch and roll trajectories, including the maximum absolute angle error for each cycle.

TABLE IV: Table of all the follower mass configurations, with the parameters for follower mass m and follower COM z offset ρ_3 .

Configuration	m [g]	ρ_3 [mm]	I [kg m ⁻²]	Image
No Mass	67	6.7	$\begin{bmatrix} 3.3 \times 10^{-5} & 0 & 0 \\ 0 & 3.1 \times 10^{-5} & 0 \\ 0 & 0 & 1.4 \times 10^{-5} \end{bmatrix}$	
+100 g	170	49	$\begin{bmatrix} 1.3 \times 10^{-4} & 0 & 0 \\ 0 & 1.3 \times 10^{-4} & 0 \\ 0 & 0 & 4.6 \times 10^{-5} \end{bmatrix}$	
+200 g	220	50	$\begin{bmatrix} 1.7 \times 10^{-4} & 0 & 0 \\ 0 & 1.7 \times 10^{-4} & 0 \\ 0 & 0 & 7.7 \times 10^{-5} \end{bmatrix}$	
+300 g	320	50	$\begin{bmatrix} 2.0 \times 10^{-4} & 0 & 0 \\ 0 & 2.0 \times 10^{-4} & 0 \\ 0 & 0 & 1.1 \times 10^{-4} \end{bmatrix}$	

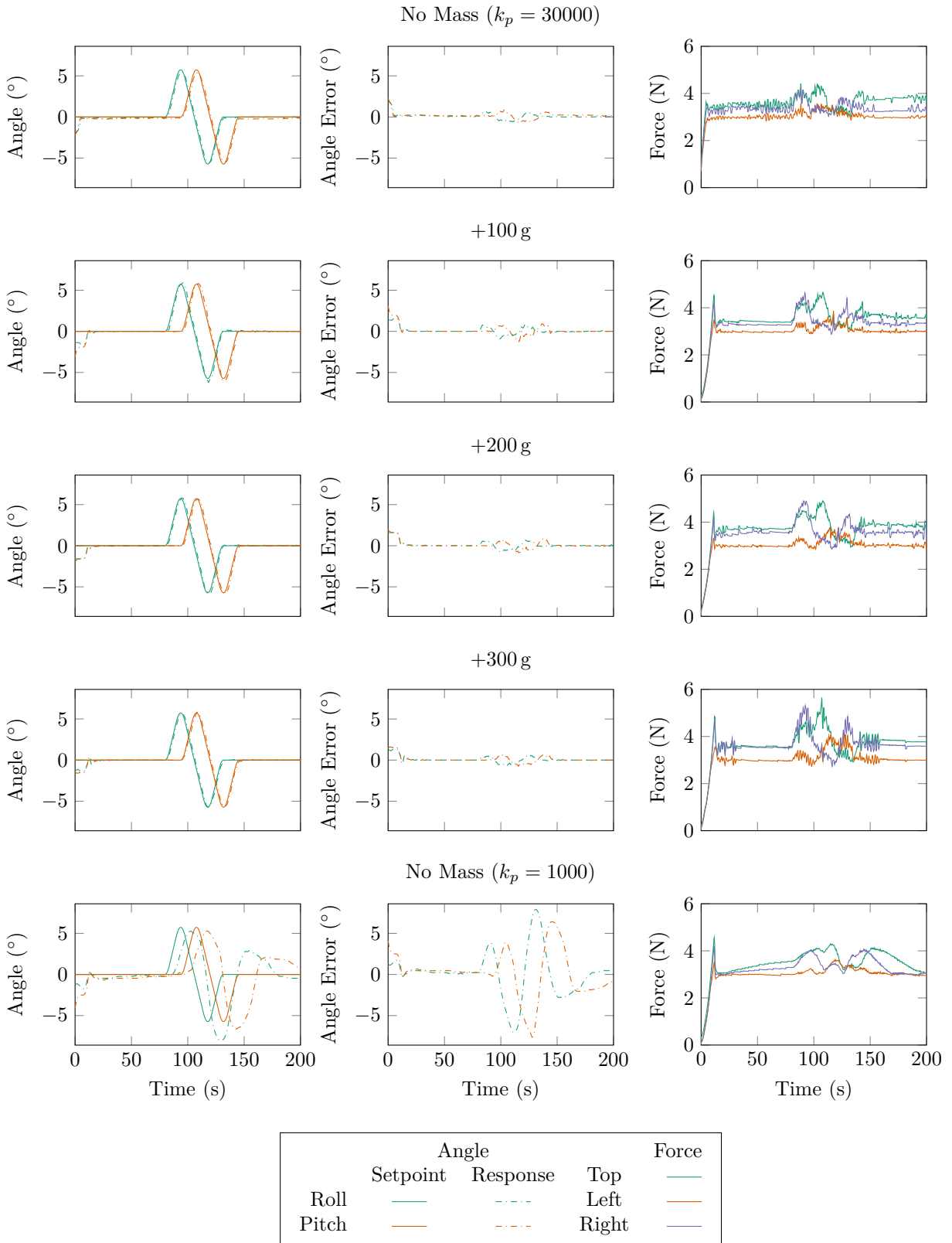


Fig. 19: AUJ pitch and roll tracking from figure 13 with increasing follower mass from table IV, as well as two different values of k_p for the “No Mass” configuration.

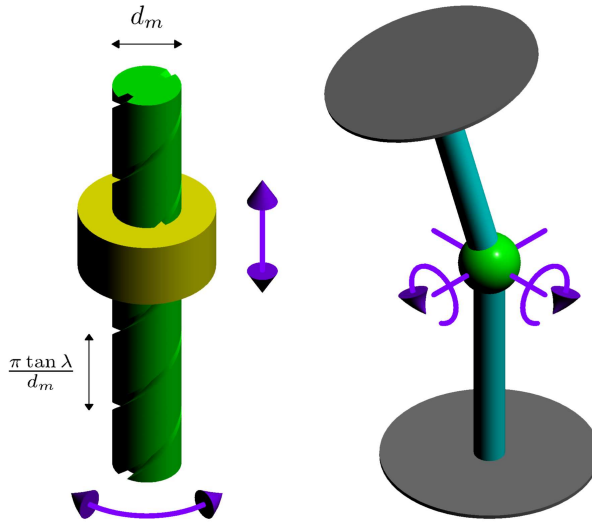


Fig. 20: Abstract diagram of a leadscrew (left) and direct drive system (right). As the screw rotates, the travelling nut moves up and down, creating a linear actuator. The direct drive employs rotary actuators to change the orientation of the AUJ directly.

$$\begin{aligned}
 k(\theta) &= l_u - \sqrt{l_u^2 - \theta_s^2 r_s^2} \\
 k^{-1}(p) &= \pm \frac{\sqrt{p(2l_u - p)}}{r_s} \\
 h^{-1}(\theta) &= \frac{\sqrt{l_n^2 - r_s^2 \theta^2}}{r_s^2 \theta} \\
 f(p) &= h^{-1}(k^{-1}(p)) = \pm \frac{\sqrt{(l_u - p)^2}}{r_s \sqrt{p(2l_u - p)}} \\
 f_{max} &= f(p)\tau_{max},
 \end{aligned} \tag{9}$$

and \dot{p}_{max} is calculated as

$$\begin{aligned}
 k(\dot{\theta}, \theta) &= \frac{\dot{\theta} r_s^2 \theta}{\sqrt{l_n^2 - r_s^2 \theta^2}} \\
 \dot{p}(\dot{\theta}, p) &= k(\dot{\theta}, k^{-1}(p)) = \pm \frac{\dot{\theta} r_s \sqrt{p(2l_n - p)}}{\sqrt{(l_n - p)^2}} \\
 \dot{p}_{max} &= \dot{p}(\dot{\theta}_{max}, p).
 \end{aligned} \tag{10}$$

2) Leadscrew: For the leadscrew metrics, the raising torque calculation [31] can be used as the absolute value of f_{max} , since the TSA only operates in tension, which can be used to determine the same metrics. The performance of different screw diameters d_m and leads λ can then be compared for a given τ_{max} and coefficient of friction μ . \dot{p}_{max} is then calculated by multiplying λ with $\dot{\theta}_{max}$. The performance of different λ can then be compared for a given $\dot{\theta}_{max}$. f_{max} is calculated as

$$\begin{aligned}
 |\tau(f)| &= \frac{d_m f (\lambda + \pi d_m \mu)}{2(\pi d_m - \lambda \mu)} \\
 |f(\tau)| &= \frac{2\tau(\pi d_m - \lambda \mu)}{d_m (\lambda + \pi d_m \mu)} \\
 f_{max} &= |f(\tau_{max})|,
 \end{aligned} \tag{11}$$

and \dot{p}_{max} is calculated as

$$\begin{aligned}
 \dot{p}(\dot{\theta}) &= \lambda \frac{\dot{\theta}}{2\pi} \\
 \dot{p}_{max} &= \dot{p}(\dot{\theta}_{max}).
 \end{aligned} \tag{12}$$

3) Direct Drive: The direct drive metrics are trivially calculated using the lever force and tangential velocity that would be generated at the endpoint of a linear actuator able to impart equivalent angular velocity and torque on the universal joint. f_{max} is calculated as

$$f_{max} = \frac{\tau_{max}}{\sqrt{l_2^2 + r^2}}, \tag{13}$$

and \dot{p}_{max} is calculated as

$$\dot{p}_{max} = \dot{\theta}_{max} \sqrt{l_2^2 + r^2}. \tag{14}$$

4) Comparison between TSA and Leadscrew: As the values for τ_{max} and $\dot{\theta}_{max}$ for the TSA depend on p , but remain constant for the leadscrew, the performance of the TSA is going to be better or worse than a given leadscrew depending on the value p . Figure 21 compares the TSA configuration using the coefficients from table I against a number of common leadscrew configurations that are practical for the dimensions of the AUJ. The TSA outperforms or underperforms different leadscrew configurations depending on p . In simpler terms, the performance of the TSA is dependent on the contraction length. The maximum linear velocity increases with the contraction length, and the maximum tension force decreases with contraction length, both in a nonlinear fashion.

B. Monofilament Torsion Fatigue & String Breakage

TSA string breakage was common during experiments, this was often due to a loss of control stability during tuning, or operation beyond previously explored motor angle or load limits. However, failure rates were observed to increase with the number of working cycles (winding and unwinding) of each TSA string, particularly when taken to high motor angles or loads. Nylon monofilament, as was used for the TSA string, is susceptible to torsion fatigue [32], [33] which reduces tensile strength [34]. This decrease in strength could be a potential explanation for the increase in failure rate. There was also the route and securing method of the string itself, which used four grub screws to clamp onto the string to hold both ends in place, and also passed close to six potentially sharp edges, as shown in figure 22. These locations could weaken the string, by either an edge biting into it when under high tension, or when being clamped by the grub screws.

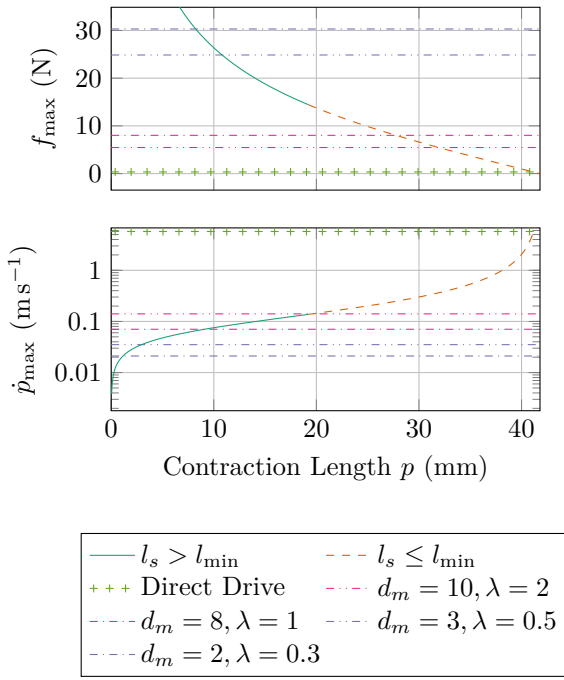


Fig. 21: Performance comparison of the TSA configuration using coefficients from table I to various leadscrew configurations with different d_m and λ , and the direct drive, where $\mu = 0.1$ for the leadscrews.

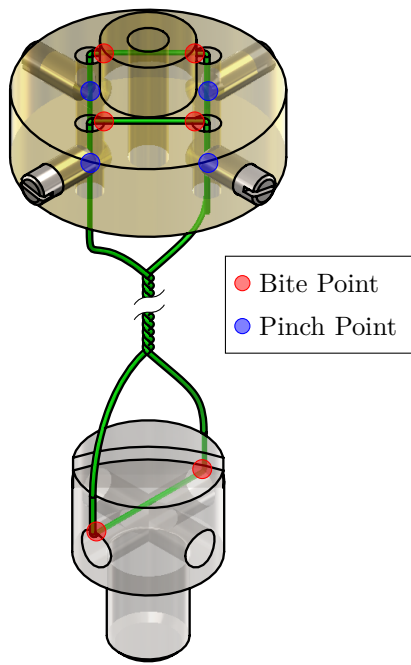


Fig. 22: Cutaway of a single TSA string assembly, including the capstan and string mount, highlighting the “pinch” points and “bite” points that could cause weaknesses in the string material, which may lead to premature failure.

The cause of the string break could be determined by the location of the break. If it was located at or near one of the grub screws or biting edges, then it was likely to be caused by those. If it was located on the “active” part of the string that twists, then torsion fatigue is likely to be the culprit. To somewhat mitigate the biting and clamping issue, polytetrafluoroethylene (PTFE) sleeving was added around the string near those locations, and this did result in a significant reduction in string breakages due to edge biting or clamping. This could be improved upon by redesigning the string clamp and capstan to round off sharp edges, and to consider alternatives to clamping such as end knotting or loop wrapping.

The experiments in [12] used 0.2 mm Dyneema® and Fast Flight® Plus polyethylene (PE) polyfilament, and were able to achieve over 1000 working cycles before failure at a load of ≤ 20 N at a motor angle of nearly 300 rad. Use of nylon monofilament was due to difficulties assembling the current design using polyfilament, as slicing the ends usually resulted in individual fibres splaying, which made it impossible thread through the string clamp. A redesign of the string clamp could make it easier to use polyfilament, which based on the results from [12] could greatly improve string longevity.

C. Improving AUJ Angle Range & Enabling Active Transmission Adjustment by Reducing Triad Radius

As can be seen in figure 23, decreasing the triad radius r decreases the stroke range of each TSA for a given AUJ angle range. This increases the AUJ angle range limits without having to increase f_{\min} as was done in section IV-C2.

If r or the AUJ angle range is small enough, this allows for active transmission adjustment, where increasing or decreasing f_{\min} shifts the active TSA stroke “window” to the right or left along the maximum force and maximum velocity curves from figure 21, as shown in figure 24. This would allow the performance of the AUJ to be adjusted during operation, which could be useful in some applications, such as a mobile snake robot which could increase AUJ angular velocity when all segments are on the ground, and sacrifice angular velocity in some segments for increased AUJ torque when they are off the ground and therefore subject to gravitational forces.

An issue with a small triad radius is the difficulty of accommodating the central shaft with the universal joint. This can be solved by using a wide universal joint with a hollow spider, which allows the three TSA to pass through the middle of the joint and the central shaft is not required, as shown in figure 25.

D. Hardware Improvements

Using the BNO080 as the AUJ orientation sensor proved to be challenging. The magnetometer was unusable within the indoor experimental environment even after several calibration attempts due to hard and soft iron biases from other components and objects near the experimental

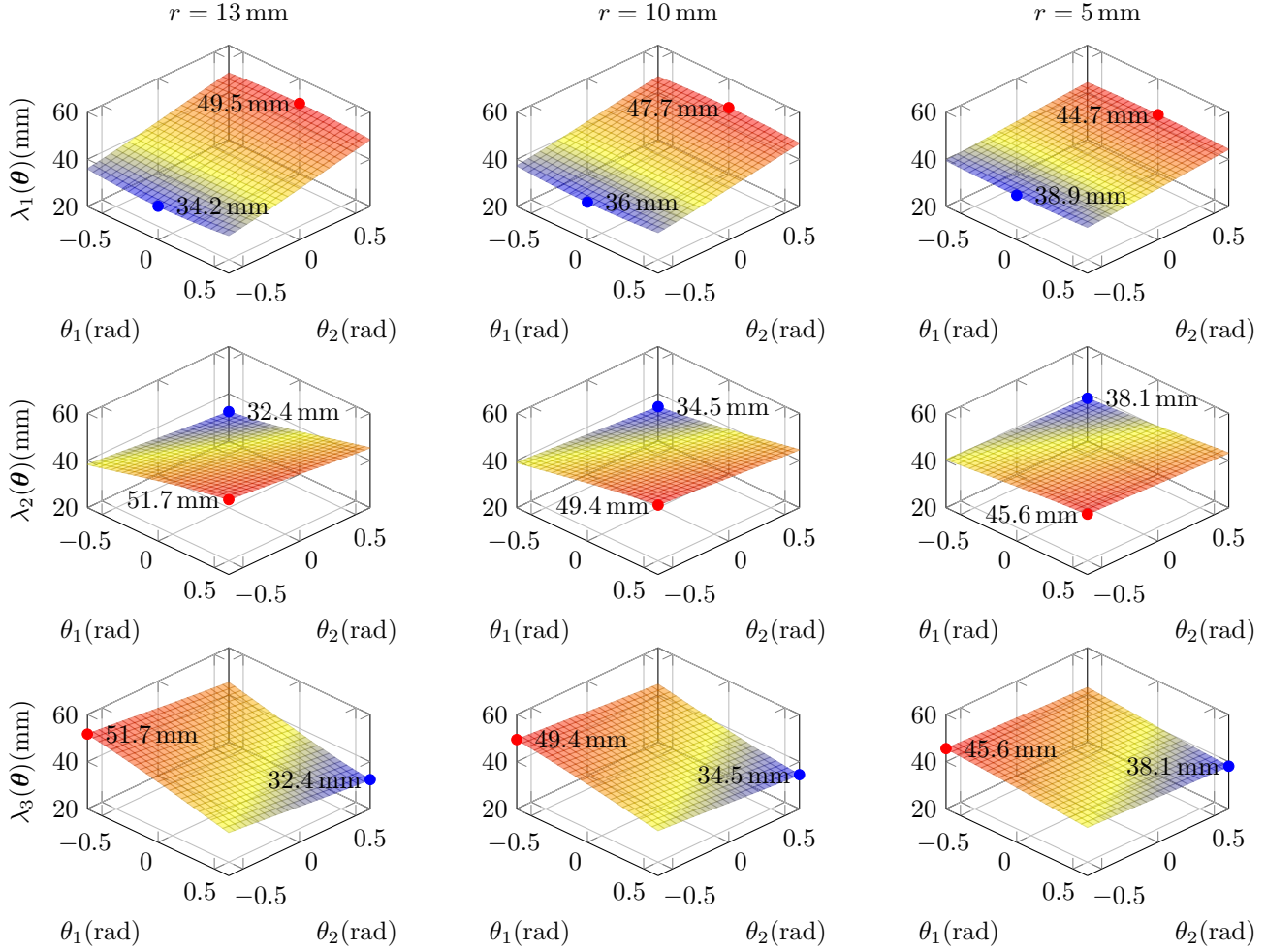


Fig. 23: Surface plots, minima and maxima for the lengths of $\lambda_{1,2,3}$ at $r = 13 \text{ mm}$, $r = 10 \text{ mm}$ and $r = 5 \text{ mm}$ in the range $[-\frac{\pi}{5}, \frac{\pi}{5}]$. As r decreases, the difference between the minima and maxima also decreases. This means that a lower value of r requires a smaller stroke range of the TSA for a given AUJ angle range.

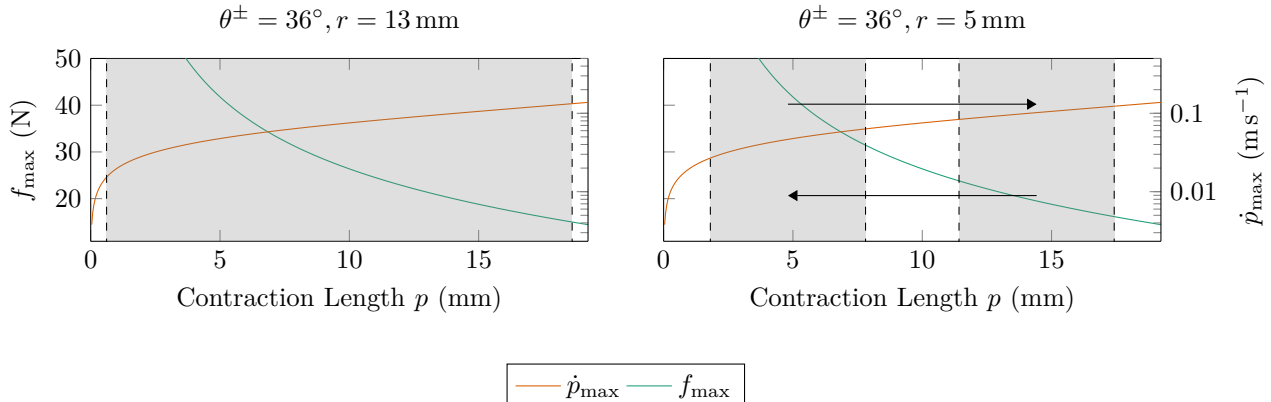


Fig. 24: By decreasing r , not only can the AUJ angle range be increased by reducing the TSA stroke range, which is marked in grey, but by adjusting f_{\min} , the transmission ratio of the TSA can be altered. Reducing f_{\min} increases the maximum TSA force f_{\max} while reducing the maximum TSA stroke velocity \dot{p}_{\max} . Conversely, increasing f_{\min} reduces f_{\max} and increases \dot{p}_{\max} . This can be used to actively modify the dynamic properties of the AUJ during operation.

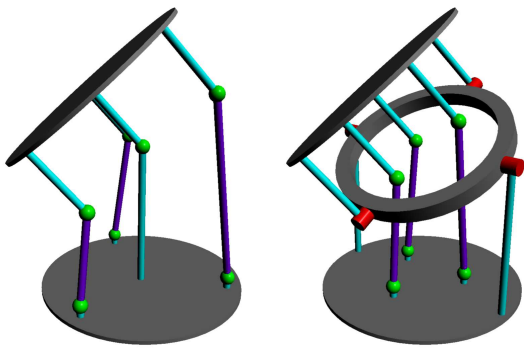


Fig. 25: An AUJ with a central universal joint, and one with a hollow spider. The hollow spider allows r to be decreased as space is no longer required for a central universal joint.

area, so the universal joint angle would not be able to be calculated when the gravity vector is not orthogonal to the universal joint DOF, hence the experiments had the AUJ in a vertical orientation. The accelerometer data from the IMU, used to calculate the AUJ orientation, was of poor resolution as can be seen in figure 26.

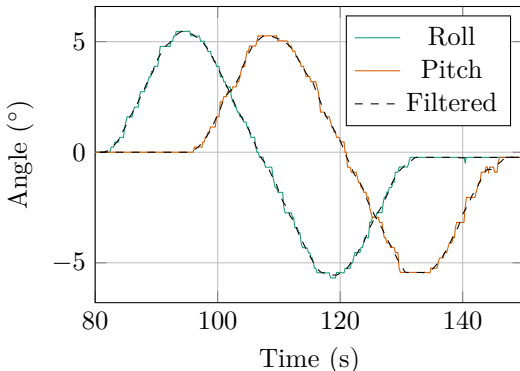


Fig. 26: Graph showing the AUJ orientation calculated from the raw IMU data, and smoothed data with the Savitsky-Golay filter applied.

An alternative method for sensing the AUJ orientation could be used, such as linear variable differential transformers (LVDTs), hall effect sensors or potentiometers. If the hollow spider universal joint design in section V-C is used, the larger spider pins would be able to accommodate potentiometers. The 1724TSR motors also had poor performance at low speeds, necessitating the deadband compensator. The use of similar size and torque brushless motors with sinusoidal commutation for stable low speed control could eliminate the need for the compensator, and allow for smoother AUJ motion.

E. Alternative Control Algorithm

Alternative control algorithms that are less or not dependant on the dynamic properties of the follower segments (mass and inertia) will also be considered, in order

to improve the robustness of the control system to external forces.

F. Multiple Segments

Development of a system comprised of multiple segments is the eventual goal of the research, to demonstrate its suitability for applications such as mobile snake robots or snake-arm robots. This can use a embedded controller for each segment, controlled by a primary controller for individual joint control or inverse kinematics, as in figure 27.

VI. CONCLUSION

This research has successfully demonstrated force based control of the orientation of a universal joint using TSA in an antagonistic triad configuration, at various velocities and follower loads. It has also compared the performance of the system to alternative actuation methods, and found that its non-linear nature makes it difficult to directly compare to similar linear actuators in the same application. Finally, it has examined the limitations of the current design, and has proposed design modifications to improve range and accuracy.

In this research, a light, compact and adaptable method for electrically actuating a universal joint using inline actuators has been conceptualised, tested and evaluated using various performance characteristics. This method has numerous potential applications in mobile robotics and robotic manipulators where a soft-rigid mechanism is required, such as mobile snake robots, snake-arm robots or robotic tails.

VII. ACKNOWLEDGEMENT

This work was supported by a UKRI EPSRC Doctoral Training Partnership [1957210], and by the UKRI Strength in Place Fund [84646 (AMPI)]. The lead author also wishes to thank Dr. Dmitriy Makhnovskiy for his assistance in preliminary research for this publication.

REFERENCES

- [1] R. Buckingham and A. Graham, "Nuclear snake-arm robots," *Industrial Robot: An International Journal*, 2012.
- [2] M. Luo, R. Yan, Z. Wan, et al., "Orisnake: Design, fabrication, and experimental analysis of a 3-d origami snake robot," *IEEE Robotics and Automation Letters*, vol. 3, no. 3, pp. 1993–1999, 2018.
- [3] W. S. Rone, W. Saab, and P. Ben-Tzvi, "Design, Modeling, and Integration of a Flexible Universal Spatial Robotic Tail," *Journal of Mechanisms and Robotics*, vol. 10, no. 4, Apr. 2018, 041001, ISSN: 1942-4302. doi: 10.1115/1.4039500.
- [4] A. Rezaei, Y. Shekofteh, M. Kamrani, A. Fallah, and F. Barazandeh, "Design and control of a snake robot according to snake anatomy," in *2008 International Conference on Computer and Communication Engineering*, IEEE, 2008, pp. 191–194.

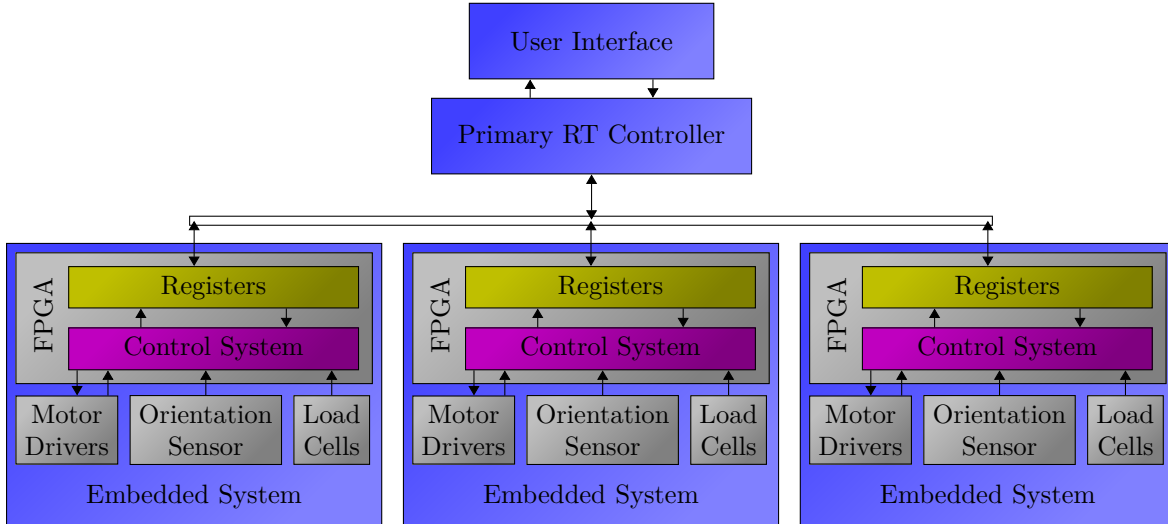


Fig. 27: Proposed system architecture for a future multi-segment system. Each segment has an embedded FPGA controller programmed with the cascaded control loop in section II. The FPGA interfaces with the load cells for each TSA, the orientation sensor for the AUJ, and the drivers for the TSA motors (the FPGA may include some motor control for a more compact design). A primary real-time controller then uses a common control bus to interface with the embedded controllers, reading and writing FPGA registers to issue motion commands and get status updates.

- [5] T. Baba, Y. Kameyama, T. Kamigawa, and A. Gofuku, “A snake robot propelling inside of a pipe with helical rolling motion,” in *Proceedings of SICE Annual Conference 2010*, IEEE, 2010, pp. 2319–2325.
- [6] C. Wright, A. Buchan, B. Brown, *et al.*, “Design and architecture of the unified modular snake robot,” in *2012 IEEE international conference on robotics and automation*, IEEE, 2012, pp. 4347–4354.
- [7] G. Qin, Y. Cheng, A. Ji, *et al.*, “Research on the cable-driven endoscopic manipulator for fusion reactors,” *Nuclear Engineering and Technology*, 2023.
- [8] T. Würtz, C. May, B. Holz, C. Natale, G. Palli, and C. Melchiorri, “The twisted string actuation system: Modeling and control,” in *2010 IEEE/ASME International Conference on Advanced Intelligent Mechatronics*, Jul. 2010, pp. 1215–1220. doi: 10.1109/AIM.2010.5695720.
- [9] P. Muehlbauer, M. Schimbera, K. Stewart, and P. P. Pott, “Twisted string actuation for an active modular hand orthosis,” in *ACTUATOR; International Conference and Exhibition on New Actuator Systems and Applications 2021*, VDE, 2021, pp. 1–4.
- [10] J. Park, J.-i. Park, H.-T. Seo, Y. Liu, K.-S. Kim, and S. Kim, “Control of tendon-driven (twisted-string actuator) robotic joint with adaptive variable-radius pulley,” in *2020 20th International Conference on Control, Automation and Systems (ICCAS)*, IEEE, 2020, pp. 1096–1098.
- [11] B. Suthar and S. Jung, “Design and feasibility analysis of a foldable robot arm for drones using a twisted string actuator: Frad-tsa,” *IEEE Robotics and Automation Letters*, vol. 6, no. 3, pp. 5769–5775, 2021. doi: 10.1109/LRA.2021.3084890.
- [12] G. Palli, C. Natale, C. May, C. Melchiorri, and T. Würtz, “Modeling and control of the twisted string actuation system,” *IEEE/ASME Transactions on Mechatronics*, vol. 18, no. 2, pp. 664–673, 2012.
- [13] R. Budynas and J. Nisbett, *Shigley’s Mechanical Engineering Design* (McGraw-Hill series in mechanical engineering). McGraw-Hill, 2011, pp. 416–417, ISBN: 9780071328401.
- [14] S. Nedelchev, I. Gaponov, and J. Ryu, “Accurate dynamic modeling of twisted string actuators accounting for string compliance and friction,” *IEEE Robotics and Automation Letters*, vol. 5, no. 2, pp. 3438–3443, 2020. doi: 10.1109/LRA.2020.2970651.
- [15] S. Nedelchev, I. Gaponov, and J.-H. Ryu, “Design of robotic gripper with constant transmission ratio based on twisted string actuator: Concept and evaluation,” in *2018 IEEE/RSJ International Conference on Intelligent Robots and Systems (IROS)*, IEEE, 2018, pp. 967–972.
- [16] M. F. Rahman, K. Zhang, and G. Herrmann, “Modular, underactuated anthropomorphic robot hand with flexible fingers and twisted string actuators,” in *Towards Autonomous Robotic Systems: 20th Annual Conference, TAROS 2019, London, UK, July 3–5, 2019, Proceedings, Part II 20*, Springer, 2019, pp. 489–492.
- [17] V. Skvortsova, S. Nedelchev, J. Brown, I. Farkhatdinov, and I. Gaponov, “Design, characterisation and validation of a haptic interface based on twisted string actuation,” *Frontiers in Robotics and AI*, vol. 9, p. 977367, 2022.

- [18] M. Usman, B. Suthar, H. Seong, E. Hawkes, I. Gaponov, and J.-H. Ryu, "Passive returning mechanism for twisted string actuators," in *2017 IEEE International Conference on Robotics and Automation (ICRA)*, IEEE, 2017, pp. 3714–3719.
- [19] D. Popov, I. Gaponov, and J.-H. Ryu, "Bidirectional elbow exoskeleton based on twisted-string actuators," in *2013 IEEE/RSJ International Conference on Intelligent Robots and Systems*, IEEE, 2013, pp. 5853–5858.
- [20] J. Park, J. H. Kim, K.-S. Kim, and S. Kim, "Design and control of antagonistic robot joint with twisted string actuators," in *2016 13th International Conference on Ubiquitous Robots and Ambient Intelligence (URAI)*, IEEE, 2016, pp. 563–565.
- [21] D. Lee, D. H. Kim, C. H. Che, J. B. In, and D. Shin, "Highly durable bidirectional joint with twisted string actuators and variable radius pulley," *IEEE/ASME Transactions on Mechatronics*, vol. 25, no. 1, pp. 360–370, 2019.
- [22] R. Konda, D. Bombara, E. Chow, and J. Zhang, "Kinematic modeling and open-loop control of a twisted string actuator-driven soft robotic manipulator," *Journal of Mechanisms and Robotics*, pp. 1–18, 2023.
- [23] D. Crosby, J. Carrasco, W. Heath, and A. Weightman, "A novel triad twisted string actuator for controlling a two degrees of freedom joint: Design and experimental validation," in *2022 International Conference on Robotics and Automation (ICRA)*, IEEE, 2022, pp. 11388–11394.
- [24] T. Sonoda and I. Godler, "Position and force control of a robotic finger with twisted strings actuation," in *2011 IEEE/ASME International Conference on Advanced Intelligent Mechatronics (AIM)*, IEEE, 2011, pp. 611–616.
- [25] D. Schlesiger, G. A. Giacoppo, M. B. Schäfer, and P. P. Pott, "Twisted string actuation with position feedback for robotic endoscopy," *Current Directions in Biomedical Engineering*, vol. 7, no. 2, pp. 343–346, 2021.
- [26] M. W. Spong, S. Hutchinson, and M. Vidyasagar, *Robot modeling and control*. John Wiley & Sons, 2020.
- [27] F. Dessen, "Coordinating control of a two degrees of freedom universal joint structure driven by three servos," in *Proceedings. 1986 IEEE International Conference on Robotics and Automation*, vol. 3, Apr. 1986, pp. 817–822. doi: 10.1109/ROBOT.1986.1087559.
- [28] *Dc micromotors - precious metal commutation*, Dr. Fritz Fauhaber GmbH & Co. KG, Feb. 2020.
- [29] *Lcm100 miniature in line load cell*, FUTEK Advanced Sensor Technology Inc.
- [30] *8-/6-/4-channel das with 16-bit, bipolar input, simultaneous sampling adc*, F, Analog Devices.
- [31] J. Shigley, C. Mischke, and R. Budynas, *Mechanical Engineering Design* (McGraw-Hill series in mechanical engineering). McGraw-Hill, 2004, ISBN: 9780072520361.
- [32] B. Goswami and J. Hearle, "A comparative study of nylon fiber fracture," *Textile Research Journal*, vol. 46, no. 1, pp. 55–70, 1976.
- [33] M. Toney and P. Schwartz, "Bending and torsional fatigue of nylon 66 monofilaments," *Journal of applied polymer science*, vol. 46, no. 11, pp. 2023–2032, 1992.
- [34] D. Hennessey, E. Carey, C. Simms, A. Hanly, and D. Winter, "Torsion of monofilament and polyfilament sutures under tension decreases suture strength and increases risk of suture fracture," *Journal of the Mechanical Behavior of Biomedical Materials*, vol. 12, pp. 168–173, 2012.



Dr. Damian J. Crosby is a Post Doctoral Research Associate in the Department of Mechanical, Aerospace and Civil Engineering, University of Manchester, U.K. He received a B.Sc. in Special Effects Development from The University of Bolton, U.K., in 2010, and a M.Res. in Robotics from The University of Plymouth, U.K., in 2012. He worked as a Research Technician in robotic laser welding at The University of Manchester from 2013 to 2017, and then completed his PhD at the same university in 2023, developing a robotic tail for improved robot balance when carrying a payload. He has worked on robotic research in the fields of nuclear energy and advanced manufacturing.



Dr. Joaquin Carrasco is a Lecturer at the Department of Electrical and Electronic Engineering, University of Manchester, UK. He was born in Abarn, Spain, in 1978. He received the B.Sc. degree in physics and the Ph.D. degree in control engineering from the University of Murcia, Murcia, Spain, in 2004 and 2009, respectively. From 2009 to 2010, he was with the Institute of Measurement and Automatic Control, Leibniz Universitt Hannover, Hannover, Germany. From 2010 to 2011, he was a Research Associate at the Control Systems Centre, School of Electrical and Electronic Engineering, University of Manchester, UK.



Prof. William P. Heath is Chair of Feedback and Control in the Department of Electrical and Electronic Engineering, University of Manchester, U.K. He received the B.A. and M.A. degrees in mathematics from Cambridge University, U.K., in 1987 and 1991, and the M.Sc. and Ph.D. degrees in systems and control from the University of Manchester Institute of Science and Technology, U.K., in 1989 and 1992, respectively. He was with Lucas Automotive from 1995 to 1998 and was a Research Academic at the University of Newcastle, Australia from 1998 to 2004. His research interests include absolute stability, multiplier theory, constrained control, and system identification.



Prof. Andrew Weightman graduated in 2006 with a PhD in Mechanical Engineering from the University of Leeds. Whilst at the University of Leeds he developed rehabilitation robotic technology for improving upper limb function in adults and children with neurological impairment which was successfully utilised in homes, schools and clinical settings. In 2013 he moved to the University of Manchester, Department of Mechanical, Aerospace and Civil Engineering as a Lecturer in Medical Mechatronics. Prof. Weightman has research interests in biomimetic mobile robotics, rehabilitation robotics, robotics for nuclear decommissioning and collaborative robotics.